ORIGINAL ARTICLE

Numerical entropy conservation without sacrificing Charney-Phillips grid optimal wave propagation

John Thuburn[1*]

[1]Department of Mathematics, University of Exeter, Exeter, EX4 4QF, UK

Correspondence
John Thuburn, Department of Mathematics, University of Exeter, Exeter, EX4 4QF, UK
Email: j.thuburn@exeter.ac.uk

Funding information
Natural Environment Research Council, Grant/Award Number: NE/N013123/1, NE/T003863/1

Conservation of entropy or potential temperature and accurate representation of wave propagation without computational modes are both desirable properties for a numerical model of the atmosphere. However, they appear to require different model formulations, forcing model developers to choose between them. Here it is shown that, by a straightforward modification of the horizontal entropy fluxes, numerical entropy conservation can be achieved without sacrificing accurate wave propagation. The result is confirmed by a numerical linear normal mode analysis for a simple but suitably modified finite volume scheme, and by buoyant bubble and gravity wave test cases in a vertical slice model using a suitably modified conservative semi-Lagrangian transport scheme.

KEYWORDS
advection; energy conservation; Lorenz grid; potential temperature; SLICE; wave dispersion

1 | INTRODUCTION

Conservative transport of entropy is a desirable property for the dynamical core of an atmospheric numerical model. So, too, is an accurate representation of wave propagation and the avoidance of computational modes. However, these two properties seem to require different model formulations, forcing model developers to choose between them. In this note a scheme for obtaining numerical entropy conservation without sacrificing optimal wave propagation is proposed and tested.

On a global scale, numerical entropy conservation is important because the entropy budget constrains the behaviour of the climate system (Goody, 2000), and it has been suggested that spurious numerical entropy production could lead to systematic biases in numerical models (Johnson, 1997). The entropy budget is closely related to the budget of available potential energy (Lorenz, 1955; Peixoto and Oort, 1992), which controls the strength of midlatitude eddies and other aspects of the circulation. The entropy budget is also important for a variety of smaller scale phenomena such as the growth of the convective boundary layer (e.g. Stull, 1988), and in precipitating convection (Emanuel et al., 1994; Pauluis and Held, 2002; Raymond, 2013). Numerical difficulties in simulating the convective boundary layer in a single-column two-fluid model, associated with the use of a non-conservative transport scheme for entropy (Thuburn et al., 2019), were a key motivation for the work presented here.

It is relatively straightforward to achieve conservation of entropy (or some related quantity such as potential temperature) in a dynamical core by formulating and discretizing its prognostic equation as a flux-form conservation law. Moreover, the developer retains considerable flexibility in how the fluxes are chosen, allowing higher-order accuracy, upwinding, and monotonicity constraints, for example.

The vertical placement of variables on the model grid can significantly affect the properties of a numerical model, including conservation properties, the propagation of marginally resolved waves, and the ability to represent balanced flows. Two main alternatives are the Charney-Phillips vertical staggering (Charney and Phillips, 1953), in which the entropy η is staggered vertically relative to the density ρ and horizontal velocity components u and v, and the Lorenz vertical staggering (Lorenz, 1960), in which the entropy is located at the same vertical levels as the density and horizontal velocity. The extensions of these two grids to the fully compressible nonhydrostatic case are shown in figure 1.

By predicting η at the same grid location as ρ, the Lorenz grid facilitates the development of schemes that conserve entropy and also energy. However, studies of the effects of grid staggering on wave propagation (e.g. Tokioka, 1978; Lesley and Purser, 1992; Fox-Rabinovitz, 1994, 1996; Thuburn and Woollings, 2005; Liu, 2008; Girard et al., 2014; Thuburn, 2017b) have shown that the Charney-Phillips grid gives more accurate wave propagation; provided the pressure gradient term is evaluated appropriately (Thuburn, 2006; Toy and Randall, 2007), the wave propagation is 'optimal' in the sense that it is as good as can be achieved by any scheme based on two-point second-order centred differences. Moreover, the Lorenz grid supports a computational mode, that is, a vertical pattern in the thermodynamic variables that spuriously satisfies hydrostatic balance and so is invisible to the dynamics. The existence of the computational mode can lead to the appearance of vertical grid scale noise, an unphysical response to forcing (e.g. Schneider, 1987), and even to spurious baroclinic instability (Arakawa and Moorthi, 1988). The reduced accuracy of wave prop-

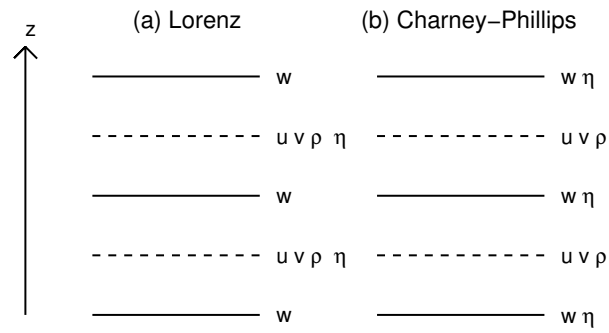

FIGURE 1 Schematic showing the vertical placement of prognostic variables (density ρ, specific entropy η, vertical velocity w, and horizontal velocity components u and v) on (a) a Lorenz grid and (b) a Charney-Phillips grid in a height based vertical coordinate.

propagation on the Lorenz grid is associated with impaired adjustment towards hydrostatic and geostrophic balance for disturbances with small vertical scale (e.g. Arakawa and Konor, 1996), and with a reduction in the effective Rossby deformation radius, implying an increased susceptibility to the so-called Hollingsworth instability (Hollingsworth et al., 1983; Bell et al., 2017) for models using the vector invariant form of the momentum equation.

On the Lorenz grid the calculation of the buoyancy term in the vertical momentum equation requires η to be vertically averaged from its native levels to w-levels. Also, if the entropy equation is written in advective form then the vertical velocity w must be averaged vertically to ρ-levels to calculate $w\,\partial\eta/\partial z$. Less obviously, if the entropy equation is written in conservative form, there is still an implied averaging of w (Appendix A). This averaging is responsible for the less accurate wave propagation, reduced effective Rossby deformation radius, and computational mode of the Lorenz grid, and the avoidance of such averaging is critical for the good wave propagation behaviour of the Charney-Phillips grid.

So, is it not possible to obtain conservation of entropy together with accurate wave propagation by using a Charney-Phillips staggering of variables combined with a flux-form discretization of the entropy equation? At first glance this does not seem to be possible. All of the studies showing accurate wave propagation on the Charney-Phillips grid assume the advective form for the entropy or potential temperature equation. If the entropy equation is written in flux form then w must be vertically averaged to compute the vertical entropy fluxes (and there is a further implied vertical averaging from the discrete product rule, Appendix A). Thus it appears impossible to avoid the unwanted vertical averaging if the entropy equation is solved in flux form, even on a Charney-Phillips grid.

The key to obtaining entropy conservation without losing the optimal Charney-Phillips grid wave propagation is to take a finite volume perspective of the behaviour of a vertical-grid-scale disturbance, and recognise that the entropy tendency in an η-cell should arise primarily through horizontal rather than vertical fluxes (section 2). This insight

then suggests a straightforward modification to a finite volume entropy transport scheme that gives it the desired properties. A numerical normal mode analysis of the discrete linearized equations confirms that such a modified finite volume scheme does indeed give optimal wave propagation (section 2).

Once this key idea is recognized, it can be adapted and applied to other conservative advection schemes. In section 3 it is applied to the conservative semi-Lagrangian SLICE scheme of Zerroukat et al. (2007, 2009). The procedure is not quite straightforward because the key idea refers to the calculation of fluxes whereas SLICE works in terms of remapping. This modified SLICE scheme is then tested in a two-dimensional model (section 4). The conservation properties are verified in an idealized saturated buoyant bubble test, and the accuracy of wave propagation is tested by simulating gravity waves with small vertical scale.

2 | FINITE VOLUME TRANSPORT

For the rest of this article we restrict attention to a Charney-Phillips grid in a height-based vertical coordinate. For clarity we will also restrict attention to the two-dimensional (x, z)-plane and assume uniform horizontal and vertical grid spacing Δx and Δz respectively. In this case all vertical averages between ρ-levels and w-levels (indicated by overbar) can be taken to have simple $^1/_2$ – $^1/_2$ weights.

A spatially discrete conservation law for mass may be written

$$\frac{\partial}{\partial t}\rho_{ij} + \frac{F^x_{i+1/2\,j} - F^x_{i-1/2\,j}}{\Delta x} + \frac{F^z_{ij+1/2} - F^z_{ij-1/2}}{\Delta z} = 0. \tag{1}$$

Here i and j are the horizontal and vertical grid indices of the cell of interest. $F^x_{i+1/2\,j}$ are the horizontal mass fluxes. The index $i + 1/2$ indicates that they are evaluated at the lateral faces of the cell, and they will typically be expressed as $F^x_{i+1/2\,j} = u_{i+1/2\,j}\hat{\rho}_{i+1/2\,j}$, where $\hat{\rho}$ is a cell face value of ρ that must be reconstructed from the cell average values ρ_{ij}. Similarly, $F^z_{ij+1/2}$ are vertical mass fluxes evaluated at the lower and upper cell faces, and typically expressed as $F^z_{ij+1/2} = w_{ij+1/2}\hat{\rho}_{ij+1/2}$. There is considerable freedom in how the $\hat{\rho}$'s are chosen.

We also require a discrete conservation law for entropy, but, since ρ and η are stored at different levels, this must be a conservation law for the quantity $\overline{\rho}\eta$. In order that the scheme should be able to preserve an initially uniform η, this conservation law must reduce to a conservation law for $\overline{\rho}$ that is consistent with (1) when $\eta \equiv 1$. The discrete conservation law for $\overline{\rho}$ is obtained simply by taking a vertical average of (1):

$$\frac{\partial}{\partial t}\overline{\rho}_{ij+1/2} + \frac{\overline{F^x}_{i+1/2\,j+1/2} - \overline{F^x}_{i-1/2\,j+1/2}}{\Delta x} + \frac{\overline{F^z}_{ij+1} - \overline{F^z}_{ij}}{\Delta z} = 0. \tag{2}$$

At the bottom boundary, level $1/2$, the conservation law applies in a layer of thickness $\Delta z/2$ and reduces to

$$\frac{\partial}{\partial t}\overline{\rho}_{i\,1/2} + \frac{\overline{F^x}_{i+1/2\,1/2} - \overline{F^x}_{i-1/2\,1/2}}{\Delta x} + \frac{\overline{F^z}_{i\,1} - \overline{F^z}_{i\,1/2}}{\Delta z/2} = 0, \tag{3}$$

with $\overline{\rho}_{i\,1/2} = \rho_{i\,1}$, $\overline{F^x}_{i+1/2\,1/2} = F^x_{i+1/2\,1}$, $\overline{F^z}_{i\,1} = {}^1\!/_2 F^z_{i\,3/2}$, and $\overline{F^z}_{i\,1/2} = 0$. A similar modification is made at the top boundary.)

We now seek a discrete flux-form conservation law for η. It's general form must be

$$\frac{\partial}{\partial t}\left(\overline{\rho}_{i\,j+1/2}\eta_{i\,j+1/2}\right) + \frac{G^x_{i+1/2\,j+1/2} - G^x_{i-1/2\,j+1/2}}{\Delta x} + \frac{G^z_{i\,j+1} - G^z_{i\,j}}{\Delta z} = 0, \tag{4}$$

(suitably modified at the lower and upper boundaries), where G^x and G^z are the horizontal and vertical entropy fluxes. Based on (2), we might anticipate that G^x and G^z must be related to $\overline{F^x}$ and $\overline{F^z}$.

Let us first clarify why a naive choice for G^x and G^z does not give optimal wave propagation. Consider the situation shown in figure 2(a). Suppose that there is a background stratification in which η increases with height, and that the mass fluxes F^x and F^z have an oscillation with vertical scale $2\Delta z$. In this situation the $2\Delta z$ structure in the fluxes should lead to a $2\Delta z$ structure in the η tendencies. This behaviour is correctly captured by the advective form η equation via the $w\,\partial\eta/\partial z$ term, which involves no averaging of w. However, we wish to use the flux-form η equation (4). Suppose the entropy fluxes are defined by

$$G^x_{i+1/2\,j+1/2} = \overline{F^x}_{i+1/2\,j+1/2}\hat{\eta}_{i+1/2\,j+1/2}, \tag{5}$$

$$G^z_{i\,j} = \overline{F^z}_{i\,j}\hat{\eta}_{i\,j}, \tag{6}$$

for some reconstructed η-cell face values $\hat{\eta}$. It is clear that if the mass fluxes F^x and F^z have a vertical $2\Delta z$ oscillation, as in figure 2(a), then the vertically averaged fluxes $\overline{F^x}$ and $\overline{F^z}$ will vanish and so, too, will the entropy fluxes (5) and (6). Consequently the η tendencies must vanish, and the correct behaviour is not captured.

To make progress, let us examine the entropy budget for the η-cell shown by the dotted line in figure 2(a). Because of the descent at the cell centre, the cell-average value of η should increase. However, this increase cannot occur via vertical fluxes through the lower and upper cell faces because the mass fluxes $\overline{F^z}$ vanish there. The only possibility, then, is that the increase in cell-average η occurs via horizontal fluxes. Now, the net mass flux at the right face of the η-cell $\overline{F^x}_{i+1/2\,j+1/2}$ is zero. However, it is made up of two non-zero but cancelling contributions: ${}^1\!/_2 F^x_{i+1/2\,j}$ on the lower part of the face and ${}^1\!/_2 F^x_{i+1/2\,j+1}$ on the upper part of the face. Because of the background stratification, $F^x_{i+1/2\,j+1}$ ought to carry a greater entropy flux into the η-cell than $F^x_{i+1/2\,j}$ carries out. Thus, there should be a net horizontal flux of entropy into the η-cell even though the net horizontal mass flux vanishes.

The situation just described can be captured by a straightforward modification of the horizontal entropy fluxes:

$$G^x_{i+1/2\,j+1/2} = \overline{F^x}_{i+1/2\,j+1/2}\hat{\eta}_{i+1/2\,j+1/2} + \frac{\Delta z}{4}\left(F^x_{i+1/2\,j+1} - F^x_{i+1/2\,j}\right)\left.\frac{\partial\eta}{\partial z}\right|_{i+1/2\,j+1/2}, \tag{7}$$

$$G^z_{i\,j} = \overline{F^z}_{i\,j}\hat{\eta}_{i\,j}. \tag{8}$$

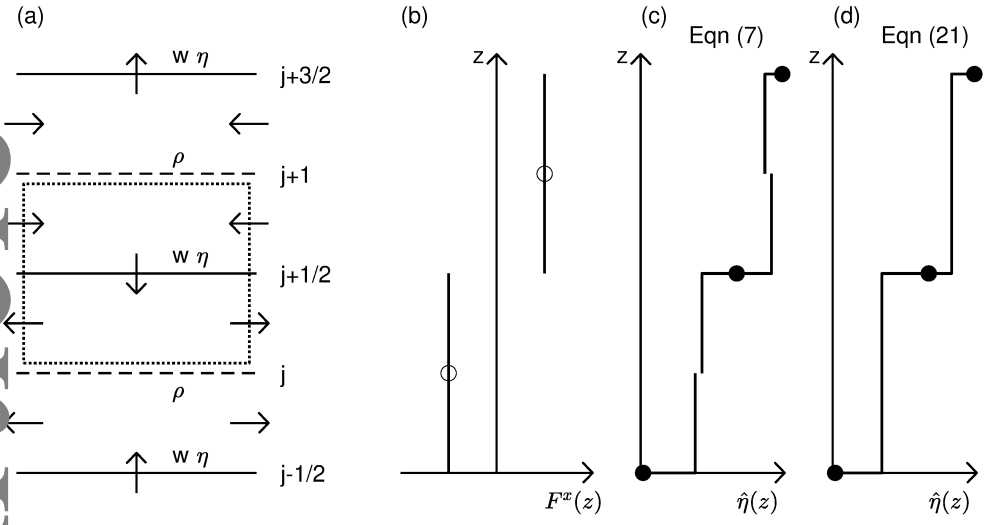

FIGURE 2 (a) Schematic showing horizontal and vertical mass fluxes (arrows) in the neighbourhood of an η grid cell (dotted line) for a disturbance with a vertical wavelength of $2\Delta z$. The vertical indices of the levels are indicated by $j, j+1/2$, etc. (b) and (c) Schematics showing the implied vertical subgrid reconstruction of the profiles of $F^x(z)$ and $\hat{\eta}(z)$ in the derivation of (7). Open circles indicate the values of F^x at ρ-levels and filled circles indicate the values of $\hat{\eta}$ at w-levels obtained by horizontal reconstruction. Note that the piecewise constant vertical reconstruction of $\hat{\eta}$ between z_j and z_{j+1} preserves the vertical average of $\hat{\eta}$ in that interval equal to $\hat{\eta}_{j+1/2}$. (d) Schematic showing the implied vertical subgrid reconstruction of $\hat{\eta}(z)$ in the derivation of (21). Note that the piecewise constant reconstruction of $\hat{\eta}$ between z_j and z_{j+1} does not preserve the vertical average of $\hat{\eta}$ in that interval equal to $\hat{\eta}_{j+1/2}$.

Here, $\partial\eta/\partial z$ is an estimate for the vertical derivative of η at the lateral cell faces, obtained, for example, using a finite difference approximation.

One way to obtain the expression (7) is as follows. For the flux $G^x_{i+1/2\,j+1/2}$, approximate the vertical profile of $F^x_{i+1/2}(z)$ by a piecewise constant subgrid reconstruction, constant between neighbouring pairs of w-levels, and the vertical profile of $\hat{\eta}_{i+1/2}(z)$ by a piecewise constant subgrid reconstruction, constant across each half-interval:

$$\hat{\eta}_{i+1/2}(z) = \begin{cases} \hat{\eta}_{i+1/2\,j+1/2} + \frac{\Delta z}{2}\left.\frac{\partial\eta}{\partial z}\right|_{i+1/2\,j+1/2}, & z_{j+1/2} \le z \le z_{j+1}; \\ \hat{\eta}_{i+1/2\,j+1/2} - \frac{\Delta z}{2}\left.\frac{\partial\eta}{\partial z}\right|_{i+1/2\,j+1/2}, & z_j \le z < z_{j+1/2}; \end{cases} \tag{9}$$

(figure 2(b),(c)). The entropy flux is then given by

$$G^x_{i+1/2\,j+1/2} = \frac{1}{\Delta z}\int_{z_j}^{z_{j+1}} F^x_{i+1/2}(z)\,\hat{\eta}_{i+1/2}(z)\,\mathrm{d}z. \tag{10}$$

Evaluating the integral then gives (7).[1]

In this argument it has been assumed that a vertical mass flux divergence in any ρ-cell is accompanied by a compensating horizontal mass flux convergence, so that the net divergence of mass flux is small. This assumption is a good approximation for the gravity waves and Rossby waves that that are adversely affected by vertical averaging of η and w. The assumption would not be a good approximation for acoustic waves, but acoustic waves are not significantly affected by vertical averaging of η or of w in the η equation. The validity of the assumption is confirmed by the numerical normal mode analysis discussed below.

It is useful to examine the implied advective form equation for η obtained by taking (4) minus $\eta_{ij+1/2}\times$(2):

$$\begin{aligned}
& \overline{\rho}_{ij+1/2}\frac{\partial}{\partial t}\eta_{ij+1/2} \\
+ \quad & \frac{1}{2}\left\{ F^x_{i+1/2j+1}\frac{\left(\hat{\eta}+\frac{\Delta z}{2}\frac{\partial\eta}{\partial z}\right)_{i+1/2j+1/2}-\eta_{ij+1/2}}{\Delta x} + F^x_{i-1/2j+1}\frac{\eta_{ij+1/2}-\left(\hat{\eta}+\frac{\Delta z}{2}\frac{\partial\eta}{\partial z}\right)_{i-1/2j+1/2}}{\Delta x}\right\} \\
+ \quad & \frac{1}{2}\left\{ F^x_{i+1/2j}\frac{\left(\hat{\eta}-\frac{\Delta z}{2}\frac{\partial\eta}{\partial z}\right)_{i+1/2j+1/2}-\eta_{ij+1/2}}{\Delta x} + F^x_{i-1/2j}\frac{\eta_{ij+1/2}-\left(\hat{\eta}-\frac{\Delta z}{2}\frac{\partial\eta}{\partial z}\right)_{i-1/2j+1/2}}{\Delta x}\right\} \\
+ \quad & \overline{F^z}_{ij+1}\frac{(\hat{\eta}_{ij+1}-\eta_{ij+1/2})}{\Delta z} + \overline{F^z}_{ij}\frac{(\eta_{ij+1/2}-\hat{\eta}_{ij})}{\Delta z} \\
= \quad & 0. \qquad (11)
\end{aligned}$$

This shows that if the fluxes have a $2\Delta z$ vertical structure and η has a background stratification, then, provided that stratification is captured by the estimates for $\partial\eta/\partial z$, there will be a non-zero tendency of η arising through the horizontal flux terms rather than the vertical flux terms. Also, if η is independent of x and the mass fluxes are approximately non-divergent (i.e., the time derivative in (1) is small) then (11) reduces to the expected form

$$\overline{\rho}_{ij+1/2}\frac{\partial}{\partial t}\eta_{ij+1/2} + F^z_{ij+1/2}\left.\frac{\partial\eta}{\partial z}\right|_{j+1/2} \approx 0. \qquad (12)$$

Finally, (11) confirms that if η is uniform, and provided $\hat{\eta}$ takes that same uniform value of η and the estimates for $\partial\eta/\partial z$ vanish, then the η tendency vanishes and the uniform value of η is preserved.

To investigate whether this modified flux-form conservation equation for η based on (7) and (8) gives the accurate wave propagation expected for the Charney-Phillips grid, a numerical linear normal mode analysis was carried out,

---

[1] As an alternative, we may use a (discontinuous) piecewise linear reconstruction for $\hat{\eta}$:

$$\hat{\eta}_{i+1/2}(z) = \hat{\eta}_{i+1/2j+1/2} + (z - z_{j+1/2})\left.\frac{\partial\eta}{\partial z}\right|_{i+1/2j+1/2},$$

and approximate the integral using the Trapezium rule, which again leads to (7). If, however, we use this piecewise linear reconstruction and evaluate the integral exactly, then we obtain an expression similar to (7) but with a factor $1/8$ rather than $1/4$. However, only with a factor $1/4$ does the implied advective form equation for η reduce to (12) in the relevant case; and only with a factor $1/4$ do we obtain optimal wave dispersion in the tests shown in figure 3. Thus, the factor $1/4$, as in (7), is indeed what is required.

following the methodology of Thuburn and Woollings (2005); Thuburn (2006). The compressible Euler equations on a β-plane, with ρ, η, u, v and w as prognostic variables, were linearized about an isothermal state of rest. The system was discretized in the vertical on a Charney-Phillips grid, and solutions proportional to $\exp\{\mathrm{i}(kx + ly - \omega t)\}$ were sought. For given values of k and l, the system comprises an eigenvalue problem for the normal mode frequencies ω and their vertical structures. In this linear calculation the values of $\hat{\eta}$ are given by the reference profile about which we linearize; thus, the details of the advection scheme do not matter, except for the inclusion of the modification (7).

Some example results are shown in figure 3 for three versions of the discrete η equation: (a) advective form; (b) naive flux form (5) and (6), and (c) modified flux form (7) and (8). For the advective form η equation the numerical frequencies agree very well with the exact frequencies for the continuous linearized equations; this result is identical to that shown by Thuburn (2006) for the same system. For the naive flux-form η equation the higher internal Rossby modes are significantly retarded due to the explicit and implicit vertical averaging of w. The modified flux form, however, captures all the wave modes with the same optimal accuracy as the advective form η equation.

Although it is the higher internal Rossby modes that are adversely affected by the averaging in the discrete equations in this example, when the horizontal wavelength is much shorter it is the higher internal gravity modes that are affected, as discussed by Thuburn (2006). The testing in section 4 below focuses on gravity waves.

3 | CONSERVATIVE SEMI-LAGRANGIAN TRANSPORT

Section 2 discusses how the fluxes should be discretized in a flux-form conservation equation for entropy so as to avoid losing the optimal wave propagation characteristics of the Charney-Phillips grid. Conservation equations can also be discretized in terms of remapping operators[2]. Such remapping-based schemes are attractive because they can be designed to be stable while remaining accurate even for large time steps. This section discusses how a such a remapping scheme can be modified so as to retain optimal wave propagation, using the SLICE transport scheme (Zerroukat et al., 2007, 2009) for illustration.

Given a set of a set of trajectory departure points for the velocity points at the faces of the ρ-cells, SLICE constructs the corresponding ρ-cell departure volumes. It then effectively carries out a multi-dimensional remapping, via a 'cascade' of one-dimensional remappings, to determine the density in the departure volumes. The mass in each departure volume is then assumed to be transported during the model time step to the corresponding arrival ρ-cell.

Figures 4(a) and 4(b) illustrate the idea in two dimensions. Using information about the grid and the departure points, SLICE constructs the departure volume (bounded by dashed lines in figure 4(b)) for each ρ-cell of the grid (bounded by solid lines in figure 4(b)). Certain Intermediate Eulerian Control Volumes are also constructed; their lateral boundaries are represented by vertical dashed lines in figure 4(a). In the first stage of SLICE the density field is remapped in the x-direction, using x as the remapping coordinate, from the ρ-cells to the Intermediate Eulerian Control Volumes.

[2] In this article the term 'remapping' is understood to imply conservation.

The mass in each Intermediate Eulerian Control Volume is assumed to equal the mass in the corresponding Intermediate Lagrangian Control Volume; the Intermediate Lagrangian Control Volumes are shown in figure 4(b), bounded laterally by dashed lines and above and below by solid lines. In the second stage of SLICE the density field is remapped from Intermediate Lagrangian Control Volumes to departure volumes. In this second stage Zerroukat et al. (2009) use z as the remapping coordinate, with Intermediate Lagrangian Control Volume upper and lower boundaries given by the z-coordinate of w-points and the departure volume upper and lower boundaries given by the z-coordinate of w departure points. However, Thuburn et al. (2010) showed that the effects of flow divergence could be captured more accurately by estimating the area of departure cells (or volume in three dimensions) using the trajectory average divergence, then using cumulative column area as the coordinate for the final remapping stage. This modification is used here too. (The freedom to choose different remapping coordinates in SLICE is discussed briefly in Appendix B.) Finally the mass in each departure volume is assumed to be transported during the time step to the corresponding arrival ρ-cell.

An obvious way to obtain conservative transport of entropy on a Charney-Phillips grid using SLICE would be to construct the departure volumes, Intermediate Eulerian Control Volumes, and Intermediate Lagrangian Control Volumes corresponding to η-cells, and then to apply the above algorithm to the quantity $\overline{\rho}\eta$ (figure 4(c),(d)). However, if we use x and column integrated area as the remapping coordinates in the first and second stages, as we do for density, then the result of transporting $\overline{\rho}\eta$ with $\eta \equiv 1$ initially is different from the result of transporting ρ followed by averaging to w-levels. Thus η will no longer be identically equal to 1 at the end of the time step; the property of preserving a constant η is lost.

The property of preserving a constant η can be recovered by again taking advantage of the freedom to choose alternative remapping coordinates. In this case we must use row integrated mass as the remapping coordinate in the first stage and column integrated mass as the remapping coordinate in the second stage. The density in η-cells is simply $\overline{\rho}$; the mass in η-cell Intermediate Control Volumes is just the vertical average of the masses in the ρ-cell Intermediate Control Volumes immediately above and below; and the mass in the η-cell departure volumes is just the vertical average of the masses in the ρ-cell departure volumes immediately above and below. From these densities and masses and the cell geometries, the required integrated mass coordinates can be straightforwardly constructed.

The resulting scheme is conservative and preserves a constant η. Unfortunately, it suffers from essentially the same problem as the naive finite volume scheme discussed in section 2: the positions of the lateral boundaries of the cell Intermediate Eulerian Control Volumes and the upper and lower boundaries of the η-cell departure volumes are determined by vertically averaged velocities, so a $2\Delta z$ pattern in the velocity is invisible to the η transport; thus the scheme does not retain the Charney-Phillips grid optimal wave propagation. We refer to this as the naive SLICE scheme in the gravity wave test of section 4.

In order to obtain optimal wave propagation, we can include a correction to the horizontal remapping of $\overline{\rho}\eta$ that is analogous to the correction to the horizontal fluxes in (7). The light shaded rectangular region in figure 4(c) represents an η-cell Intermediate Eulerian Control Volume. In the first stage of the naive SLICE scheme, $\overline{\rho}\eta$ is remapped horizontally from η-cells to these Intermediate Eulerian Control Volumes. To apply the correction, observe that the

difference of mass fluxes in the correction term in (7), integrated over a time step, corresponds to twice the sum of the two dark shaded areas in figure 4(c) (with appropriate allowance for sign) multiplied by $\hat{\rho}$, an estimate of the density at that edge of the Intermediate Eulerian Control Volume. $\hat{\rho}$ may be estimated as a by-product of the horizontal remapping of ρ. This difference of mass fluxes is multiplied by an estimate for $\partial\eta/\partial z \times \Delta z$ to obtain an entropy flux correction. An estimate for $\partial\eta/\partial z \times \Delta z$ at the edge of the Intermediate Eulerian Control Volume can be estimated as half the difference between edge values of η at the levels above and below; these edge values of η again can be obtained as by-products of the horizontal remapping. The entropy flux correction is then applied to conservatively shift entropy between neighbouring Intermediate Eulerian Control Volumes.

4 | NUMERICAL EXAMPLES

Some numerical tests were carried out to confirm the conservation and wave dispersion properties of the modified SLICE scheme. The two-dimensional moist compressible Euler equations were solved using the semi-implicit, semi-Lagrangian vertical slice model described by Thuburn (2017a). The model uses a Charney-Phillips vertical grid, with specific humidity as well as entropy stored at w-points. The original formulation uses (in its default configuration) SLICE with parabolic spline subgrid reconstruction for conservative transport of density and a semi-Lagrangian scheme with cubic Lagrange interpolation for transport of entropy, specific humidity, and w. An option to use the modified SLICE scheme for transport of entropy, specific humidity, and w was implemented and compared.

4.1 | Conservation

To test the conservation properties, the semi-Lagrangian and modified-SLICE versions were compared on the saturated buoyant bubble test case of Bryan and Fritsch (2002). The domain is 20 km wide and 10 km deep, discretized with 200×96 grid cells, giving a horizontal and vertical grid length of a little over 100 m. The time step is 10 s.

Figures 5(a) and 5(b) compare the perturbation to equivalent potential temperature θ_e for the two model versions after 800 s. There are some small but noticeable differences at the leading edge of the bubble, where the perturbation is slightly smaller for the modified-SLICE scheme. The overall evolution, however, is very similar for the two versions. At later times (e.g., figures 5(c),(d)) the differences between the two versions grow. This test case, particularly the behaviour at the leading edge of the bubble, is notoriously sensitive to details of the numerics (e.g. Duarte et al., 2014; Kurowski et al., 2014), and a similar sensitivity was found here. All of the schemes tested, semi-Lagrangian, modified SLICE, and unmodified SLICE, each with and without limiters, produced clear differences from each other at the bubble's leading edge at 1000 s.

Figures 5(e) and 5(f) compare the conservation of entropy (solid lines) and energy (dashed lines) in the semi-Lagrangian and modified-SLICE versions. Note the different axis scale in the two panels. See Appendix C for a discussion of how the entropy and energy changes are normalized. In the semi-Lagrangian version there are normalized

entropy and energy losses of around −0.15 over 1000 s, while in the modified-SLICE version entropy is conserved to machine precision. The model is not formulated to conserve energy exactly, so we should not expect perfect energy conservation even with the modified-SLICE version. Figure 5(f) shows a very slight increase in energy between 200 s and 500 s before numerical dissipation of kinetic energy becomes significant at later times. Nevertheless, as a by-product of the entropy conservation, the energy loss in the modified-SLICE version is an order of magnitude smaller than in the semi-Lagrangian version.

The total water content (not shown) is actually conserved to machine precision for both model versions in this test case. In the semi-Lagrangian version this exact conservation occurs because the specific humidity is uniform. Preservation of this uniform specific humidity by the semi-Lagrangian advection, together with conservation of mass by the SLICE transport, implies conservation of total water. For non-uniform specific humidity the semi-Lagrangian version would not conserve total water. The uniform specific humidity was also preserved to machine precision by the modified-SLICE version, confirming that the mass-coordinate-based remapping for entropy and specific humidity works as intended.

4.2 | Wave dispersion

To test the wave dispersion properties, the model was initialized with a packet of gravity waves of small vertical wavelength, and the frequency of the waves in the model was compared to the analytical frequency and the theoretical optimal numerical frequency.

As above, the domain size was 20 km×10 km with resolution 192×96 grid cells. A background resting hydrostatically balanced state with surface pressure 10^5 Pa and uniform temperature $T = 270$ K was set up. Specific humidity was set to zero. A gravity wave packet disturbance was then superposed, with the following distributions of buoyancy b and mass stream function ψ:

$$b = w_0 \frac{N^2}{\omega} \cos^2(r\pi/2) \cos(kx' + mz'), \tag{13}$$

$$\psi = \rho_c \frac{w_0}{k} \cos^2(r\pi/2) \cos(kx' + mz'). \tag{14}$$

Here

$$x' = x - x_c, \qquad z' = z - z_c, \tag{15}$$

where $(x_c, z_c) = (10^4 \text{ m}, 5 \times 10^3 \text{ m})$ is the centre of the wave packet,

$$r = \min\left(1, \sqrt{(x'/x_r)^2 + (z'/z_r)^2}\right) \tag{16}$$

with $x_r = 7 \times 10^3$ m and $z_r = 3.5 \times 10^3$ m defining the size of the wave packet, $w_0 = 0.01\,\mathrm{ms}^{-1}$ is the vertical velocity amplitude, k and m are the horizontal and vertical wavenumbers of the wave, $N^2 = g^2/c_pT$ is the background buoyancy frequency squared, with $g = 9.81\,\mathrm{ms}^{-2}$ the gravitational acceleration and $c_p = 1004\,\mathrm{Jkg}^{-1}\mathrm{K}^{-1}$ the specific heat capacity at constant pressure, and $\rho_c \approx 0.7\,\mathrm{kgm}^{-3}$ is the background density at the centre of the wave packet. The frequency for a monochromatic gravity wave is given, to a good approximation, by the Boussinesq frequency

$$\omega^2 = \frac{k^2N^2}{k^2 + m^2}. \tag{17}$$

The initial density and entropy are adjusted to give the buoyancy field specified by (13) without perturbing the pressure. The mass stream function ψ is used to construct the initial velocity field

$$\rho u = -\frac{\partial \psi}{\partial z}; \qquad \rho w = \frac{\partial \psi}{\partial x}. \tag{18}$$

The resulting disturbance evolves as a packet of nearly monochromatic gravity waves, with phase propagation towards the lower left perpendicular to phase lines, and group propagation towards the upper left, approximately parallel to phase lines, in agreement with the theory of idealized gravity waves (e.g. Vallis, 2017, section 7.3).

For well-resolved waves the numerical frequency should be close to the analytical Boussinesq frequency (17). However, for waves that are less well-resolved in space, even with optimal grid staggering, the inexact approximation of derivatives changes the frequency. For second-order centred-difference derivatives on a Charney-Phillips C-grid, as used here, the effect of the numerical errors can be quantified, and is to replace the exact frequency (17) by the (optimal) numerical frequency

$$\omega^2_{\mathrm{num}} = \frac{\hat{k}^2N^2}{\hat{k}^2 + \hat{m}^2}, \tag{19}$$

where

$$\hat{k} = \frac{\sin(k\Delta x/2)}{\Delta x/2}, \qquad \hat{m} = \frac{\sin(m\Delta z/2)}{\Delta z/2}, \tag{20}$$

are the effective wavenumbers seen by staggered centred-difference derivatives. On a Lorenz grid, or on a Charney-Phillips grid with naive flux-form transport of entropy or with a suboptimal form of the pressure gradient term, the vertical averaging of w and/or η introduces a further factor $\cos^2(m\Delta z/2)$ in (19), severely slowing the the waves that are marginally resolved in the vertical (Thuburn, 2006). For the experiments discussed here the time step $\Delta t = 10\,\mathrm{s}$ is much shorter than the wave period, so time discretization errors are negligible.

The horizontal wavenumber was fixed at $k = \pi \times 10^{-3}\,\mathrm{m}^{-1}$. For a range of vertical wavenumbers, the gravity wave packet was simulated and the empirical period of the wave was estimated from time series of u, w, and η at the centre of the domain. (This estimate incurs some small errors because attention is restricted to periods that are multiples of

TABLE 1 Exact, optimal numerical, and empirical gravity wave periods τ for a range of vertical wavenumbers m.

m (m^{-1})	Boussinesq τ (s)	Optimal numerical τ (s)	Empirical τ (s) SL	Empirical τ (s) modified SLICE	Empirical τ (s) naive SLICE
$\pi/1000$	471.6	471.6	480	480	480
$\pi/500$	745.7	737.7	750	750	790
$\pi/250$	1375.9	1290.1	1290	1290	1630
$\pi/175$	1934.5	1680.6	1670	1670	2810
$\pi/\Delta z$	3218.7	2074.1	2070	2070	$\gg 5000$

the time step, and because the wave packet propagates away so that wave amplitude at the domain centre decays over time.) The empirical period was then compared with the theoretical Boussinesq and optimal numerical periods. The results are shown in table 1. For both semi-Lagrangian and modified SLICE transport of η the wave periods agree well with the theoretical wave periods for an optimal scheme.

The same set of gravity wave simulations was carried out with η transport given by the naive SLICE scheme discussed in section 3. The results are shown in the final column of table 1. They confirm that this naive application of SLICE does not lead to optimal wave propagation. They also confirm that this test case can indeed discriminate between optimal and suboptimal wave propagation. In fact, these periods are longer than the optimal periods by the theoretical factor $1/\cos(m\Delta z/2)$.

5 | SUMMARY AND DISCUSSION

On a Charney-Phillips vertical grid, for which entropy η is staggered vertically relative to density ρ, conservation of entropy can be obtained by integrating a flux-form conservation equation for the quantity $\overline{\rho}\eta$. A naive discretization of this conservation equation involves explicit and implicit vertical averaging, so that optimal wave propagation is lost, despite the use of a Charney-Phillips grid. This article presents a straightforward and general method for modifying the horizontal fluxes in the entropy conservation equation so as to restore optimal wave propagation. An analogous modification can be made in a conservative semi-Lagrangian scheme based on remapping.

The proposed idea has been tested, and the predicted behavior confirmed, by computing numerical linear normal modes for an idealized basic state, and by simulating a saturated buoyant bubble and marginally resolved gravity waves in a two-dimensional vertical slice model.

For clarity of presentation the idea has been presented in the two-dimensional context and for a vertically uniform grid. However, it extends straightforwardly to three dimensions and to vertically non-uniform grids.

At an early stage of this work, an alternative modification of the horizontal fluxes was considered:

$$G^x_{i+1/2\,j+1/2} = \overline{F^x}^{\hat{\eta}}_{i+1/2\,j+1/2}. \tag{21}$$

In this scheme, η is first vertically averaged to ρ-levels, then used to construct values at the lateral faces of ρ-cells $\hat{\eta}_{i+1/2j}$ and hence entropy fluxes at the lateral faces of ρ-cells $F^x_{i+1/2j}\hat{\eta}_{i+1/2j}$, which are then averaged back to w-levels to give $G^x_{i+1/2j+1/2}$. Interestingly, this scheme can be obtained by a slight modification of the derivation (9), (10) using a different piecewise constant subgrid reconstruction of $\hat{\eta}_{i+1/2}(z)$:

$$\hat{\eta}_{i+1/2}(z) = \begin{cases} \frac{1}{2}\left(\hat{\eta}_{i+1/2j+1/2} + \hat{\eta}_{i+1/2j+3/2}\right), & z_{j+1/2} \le z \le z_{j+1}; \\ \frac{1}{2}\left(\hat{\eta}_{i+1/2j-1/2} + \hat{\eta}_{i+1/2j+1/2}\right), & z_j \le z < z_{j+1/2}; \end{cases} \tag{22}$$

(Figure 2(d)). This scheme is conservative and has the optimal wave dispersion property. However, it is less accurate than (7). This is most clear if we consider the case of F^x independent of z, whereupon

$$G^x_{i+1/2j+1/2} = F^x\bar{\bar{\hat{\eta}}}_{i+1/2j+1/2}. \tag{23}$$

The double vertical average of $\hat{\eta}$ is only a second-order approximation to $\hat{\eta}_{i+1/2j+1/2}$, so the scheme is, at best, second-order accurate for advection. This reduction in accuracy is noticeable in advection tests with the SLICE analogue of the scheme. On the other hand, the modification described in section 3, which is the SLICE analogue of equation (7), remains as accurate as the unmodified SLICE scheme.

The modification described in this article permits considerable flexibility in the choice of the cell-edge values $\hat{\eta}$, or in the choice of subgrid reconstruction in the case of the SLICE scheme. In particular, schemes with high order of accuracy are possible, and so are flux limiters that prevent the numerical generation of overshoots and undershoots in η. The results shown in section 4 all use a parabolic spline subgrid reconstruction for SLICE and include a limiter for the transport of entropy and water (Zerroukat et al., 2006). The results using semi-Lagrangian advection shown in table 1 use two-dimensional cubic Lagrange interpolation with a simple monotonicity limiter. Switching off the limiters makes negligible difference to the results in table 1.

In summary, the modified SLICE scheme presented here, applied to the transport of entropy on a Charney-Phillips vertical grid, achieves several desirable properties: high overall accuracy, stability at large time steps, conservation, preservation of a constant, and prevention of overshoots and undershoots. It does all this without sacrificing the optimal wave propagation permitted by the Charney-Phillips grid.

Acknowledgements

This work was funded by the Natural Environment Research Council under grants NE/N013123/1 and NE/T003863/1 as part of the ParaCon programme. The author is grateful to Nigel Wood for constructive comments on an earlier draft of this article, in particular for pointing out how the derivation of equations (7) and (21) can be understood in terms of a choice of subgrid reconstruction for $\hat{\eta}$.

A | DISCRETE DERIVATIVE OF A PRODUCT

Suppose we wish to evaluate a centred difference approximation to the product ab at level j, where a and b are quantities stored at levels $j \pm 1/2$. Let the grid spacing be Δz. Then

$$\begin{aligned}
\left.\frac{\partial(ab)}{\partial z}\right|_j &\approx \frac{1}{\Delta z}\left(a_{j+1/2}b_{j+1/2} - a_{j-1/2}b_{j-1/2}\right) \\
&= \frac{1}{2\Delta z}\left(a_{j+1/2}b_{j+1/2} - a_{j+1/2}b_{j-1/2} + a_{j-1/2}b_{j+1/2} - a_{j-1/2}b_{j-1/2}\right) \\
&+ \frac{1}{2\Delta z}\left(a_{j+1/2}b_{j+1/2} - a_{j-1/2}b_{j+1/2} + a_{j+1/2}b_{j-1/2} - a_{j-1/2}b_{j-1/2}\right) \\
&= \overline{a}_j \frac{b_{j+1/2} - b_{j-1/2}}{\Delta z} + \overline{b}_j \frac{a_{j+1/2} - a_{j-1/2}}{\Delta z},
\end{aligned} \tag{24}$$

where an overbar indicates a vertical average. Thus, the discrete centred-difference product rule contains implied vertical averages.

B | CHOICE OF REMAPPING COORDINATE FOR SLICE

Each one-dimensional remapping stage of SLICE can be formulated in terms of a general coordinate s and 'density' $q(s)$. Given a set of cell-boundary coordinates $s_{j+1/2}$ and the cell-integral values

$$Q_j = \int_{s_{j-1/2}}^{s_{j+1/2}} q(s)\, ds, \tag{25}$$

SLICE reconstructs an estimate for the subgrid distribution $q(s)$, enabling the cell-integral values to be estimated for an alternative set of cell boundaries $\tilde{s}_{j+1/2}$:

$$\tilde{Q}_j = \int_{\tilde{s}_{j-1/2}}^{\tilde{s}_{j+1/2}} q(s)\, ds. \tag{26}$$

Conservation is obtained by ensuring that

$$\sum_j Q_j = \int q(s)\, ds = \sum_j \tilde{Q}_j. \tag{27}$$

An obvious choice is to take s to be distance in some coordinate direction, say $s = x$, and q to be density times cell depth $q = \rho\Delta z$ or tracer density times cell depth $q = \rho\eta\Delta z$. This is what is done to remap density in the first stage of SLICE (figure 4(a)). (In this case the Δz factor is constant and so could be omitted.)

An analogous choice for remapping density in the second stage of SLICE would be $s = z$ and $q = \rho\delta x$, where $\delta x(z)$ is the width of the column being remapped. However, as discussed by Thuburn et al. (2010), the effects of flow

divergence can be captured more accurately by using a volume-based coordinate (in two dimensions an area-based coordinate) that incorporates the column width

$$s = \int \delta x \, dz = \int dA, \tag{28}$$

together with $q = \rho$. This area-based coordinate is used to remap density in the second stage of SLICE (figure 4(b)).

To ensure consistency with the transport of mass, and hence ensure preservation of a constant η, the transport of η uses column integrated mass as the coordinate; for the first stage

$$s = \int \rho \Delta z \, dx = \int \rho \, dA = \int dm, \tag{29}$$

and for the second stage

$$s = \int \rho \delta x \, dz = \int \rho \, dA = \int dm, \tag{30}$$

together with $q = \eta$. This choice ensures that, when $\eta \equiv 1$, the entropy content in a remapped cell agrees with the ρ content:

$$\tilde{Q}_j = \tilde{s}_{j+1/2} - \tilde{s}_{j-1/2} = \int_{\text{cell } j} \rho \, dA. \tag{31}$$

It is useful to note that the first stage of the density remapping may be re-interpreted as using row integrated area as the remapping coordinate:

$$s = \int \Delta z \, dx = \int dA. \tag{32}$$

These choices of remapping coordinate then suggest the following general rule of thumb.

- For remapping density, in order to accurately capture the effects of the velocity divergence, use integrated area (integrated volume in three dimensions) as the remapping coordinate in all stages of SLICE. The same applies when remapping the velocity divergence itself in order to compute the departure cell areas (or volumes) (Thuburn et al., 2010).
- For remapping tracer density, e.g. $\rho\eta$, in order to ensure compatibility with the density remapping and ensure preservation of constant η, use integrated mass as the remapping coordinate in all stages of SLICE.

C | NORMALIZATION OF ENTROPY AND ENERGY CHANGES

A natural way normalize the entropy and energy changes in the buoyant bubble test might appear to be to compute the fractional changes in these quantities. However, arbitrary constants may be added to the definitions of specific internal energy, potential energy, and specific entropy without changing any of the essential physics (e.g. Feistel et al., 2008). Since the diagnosed fractional change in entropy and energy will depend on the choices for these constants, the fractional change is not a unique and objective measure. Instead, we normalize the energy change by $\mathrm{KE}_{\max} \approx 1.3 \times 10^9$, the maximum domain integrated kinetic energy during the 1000 s run, and the entropy change by $\mathrm{KE}_{\max}/T_{\max}$, where $T_{\max} \approx 289.6$ K is the temperature near the surface.

references

Arakawa, A. and Konor, C. S. (1996) Vertical differencing of the primitive equations based on the Charney-Phillips grid in hybrid $\sigma - p$ vertical coordinates. *Mon. Wea. Rev.*, **124**, 511–528.

Arakawa, A. and Moorthi, S. (1988) Baroclinic instability in vertically discrete systems. *J. Atmos. Sci.*, **45**, 1688–1707.

Bell, M. J., Peixoto, P. S. and Thuburn, J. (2017) Numerical instabilities of vector-invariant momentum equations on rectangular C-grids. *Quart. J. Roy. Meteor. Soc.*, **143**, 563–581.

Bryan, G. H. and Fritsch, J. M. (2002) A benchmark simulation for moist nonhydrostatic numerical models. *Mon. Wea. Rev.*, **130**, 2917–2928.

Charney, J. G. and Phillips, N. A. (1953) Numerical integration of the quasi-geostrophic equations for barotropic and simple baroclinic flow. *J. Meteorol.*, **10**, 71–99.

Duarte, M., Almgren, A. S., Balakrishnan, K. and Bell, J. B. (2014) A numerical study of methods for moist atmospheric flows: Compressible equations. *Mon. Wea. Rev.*, **142**, 4269–4283.

Emanuel, K. A., Neelin, J. D. and Bretherton, C. S. (1994) On large-scale circulations in convecting atmospheres. *Quart. J. Roy. Meteor. Soc.*, **120**, 1111–1143.

Feistel, R., Wright, D. G., Miyagawa, K., Harvey, A. H., Hruby, J., Jackett, D. R., McDougall, T. J. and Wagner, W. (2008) Mutually consistent thermodynamic potentials for fluid water, ice and seawater: a new standard for oceanography. *Ocean Sci.*, **4**, 275–291.

Fox-Rabinovitz, M. S. (1994) Computational dispersion properties of vertically staggered grids for atmospheric models. *Mon. Wea. Rev.*, **122**, 377–392.

— (1996) Computational dispersion properties of 3D staggered grids for a nonhydrostatic anelastic system. *Mon. Wea. Rev.*, **124**, 498–510.

Girard, C., Plante, A., Desgagné, M., McTaggart-Cowan, R., Côté, J., Charron, M., Gravel, S., Lee, V., Patoine, A., Qaddouri, A., Roch, M., Spacek, L., Tanguay, M., Vaillancourt, P. A. and Zadra, A. (2014) Staggered vertical discretization of the Canadian environmental multiscale (GEM) model using a coordinate of the log-hydrostatic-pressure type. *Mon. Wea. Rev.*, **142**, 1183–1196.

Goody, R. (2000) Sources and sinks of climate entropy. *Quart. J. Roy. Meteor. Soc.*, **126**, 1953–1970.

Hollingsworth, A., Kallberg, P., Renner, V. and Burridge, D. M. (1983) An internal symmetric computational instability. *Quart. J. Roy. Meteor. Soc.*, **109**, 417–428.

Johnson, D. R. (1997) "General coldness of climate models" and the Second Law: Implications for modeling the Earth system. *J. Climate*, **10**, 2826–2846.

Kurowski, M. J., Grabowski, W. W. and Smolarkiewicz, P. K. (2014) Anelastic and compressible simulations of moist deep convection. *J. Atmos. Sci.*, **71**, 3767–3787.

Lesley, L. M. and Purser, R. J. (1992) A comparitive study of the performance of various vertical discretization schemes. *Meteor. Atmos. Phys.*, **50**, 61–73.

Liu, Y. (2008) Impact of difference accuracy on computational properties of vertical grids for a nonhydrostatic model. *Comput. Geosci.*, **12**, 245–253.

Lorenz, E. N. (1955) Available potential energy and the maintenance of the global circulation. *Tellus*, **7**, 157–167.

— (1960) Energy and numerical weather prediction. *Tellus*, **12**, 364–373.

Pauluis, P. and Held, I. M. (2002) Entropy budget of an atmosphere in radiative-convective equilibrium. Part I: Maximum work and frictional dissipation. *J. Atmos. Sci.*, **59**, 125–139.

Peixoto, J. P. and Oort, A. H. (1992) *Physics of Climate*. New York: American Institute of Physics.

Raymond, D. J. (2013) Sources and sinks of entropy in the atmosphere. *J. Adv. Model. Earth Syst.*, **5**, 755–763.

Schneider, E. K. (1987) An inconsistency in vertical discretization in some atmospheric models. *Mon. Wea. Rev.*, **115**, 2166–2169.

Stull, R. B. (1988) *An Introduction to Boundary Layer Meteorology*. Kluwer Academic.

Thuburn, J. (2006) Vertical discretizations giving optimal representation of normal modes: Sensitivity to the form of the pressure-gradient term. *Quart. J. Roy. Meteor. Soc.*, **132**, 2809–2825.

— (2017a) Use of the Gibbs thermodynamic potential to express the equation of state in atmospheric models. *Quart. J. Roy. Meteor. Soc.*, **143**, 1185–1196.

— (2017b) Vertical discretizations giving optimal representation of normal modes: General equations of state. *Quart. J. Roy. Meteor. Soc.*, **143**, 1714–1720.

Thuburn, J., Efstathiou, G. A. and Beare, R. J. (2019) A two-fluid single-column model of the dry, shear-free, convective boundary layer. *Quart. J. Roy. Meteor. Soc.*, **145**, 1535–1550.

Thuburn, J. and Woollings, T. J. (2005) Vertical discretizations for compressible Euler equation atmospheric models giving optimal representation of normal modes. *J. Comput. Phys.*, **203**, 386–404.

Thuburn, J., Zerroukat, M., Wood, N. and Staniforth, A. (2010) Coupling a mass-conserving semi-Lagrangian scheme (SLICE) to a semi-implicit discretisation of the shallow-water equations: Minimizing the dependence on a reference atmosphere. *Quart. J. Roy. Meteor. Soc.*, **136**, 146–154.

Tokioka, T. (1978) Some considerations on vertical differencing. *J. Meteor. Soc. Japan*, **56**, 98–111.

Toy, M. D. and Randall, D. A. (2007) Comment on the article "vertical discretizations for compressible Euler equation atmospheric models giving optimal representation of normal modes" by Thuburn and Woollings. *J. Comput. Phys.*, **223**, 82–88.

Vallis, G. K. (2017) *Atmospheric and Oceanic Fluid Dynamics*. Cambridge University Press, 2nd edn.

Zerroukat, M., Wood, N. and Staniforth, A. (2006) The Parabolic Spline Method (PSM) for conservative transport problems. *Int. J. Num. Methods in Fluids*, **51**, 1297–1381.

— (2007) Application of the Parabolic Spline Method (PSM) to a multidimensional conservative transport scheme (SLICE). *J. Comput. Phys.*, **225**, 935–948.

— (2009) An improved version of SLICE for conservative monotonic remapping on a C-grid. *Quart. J. Roy. Meteor. Soc.*, **135**, 541–546.

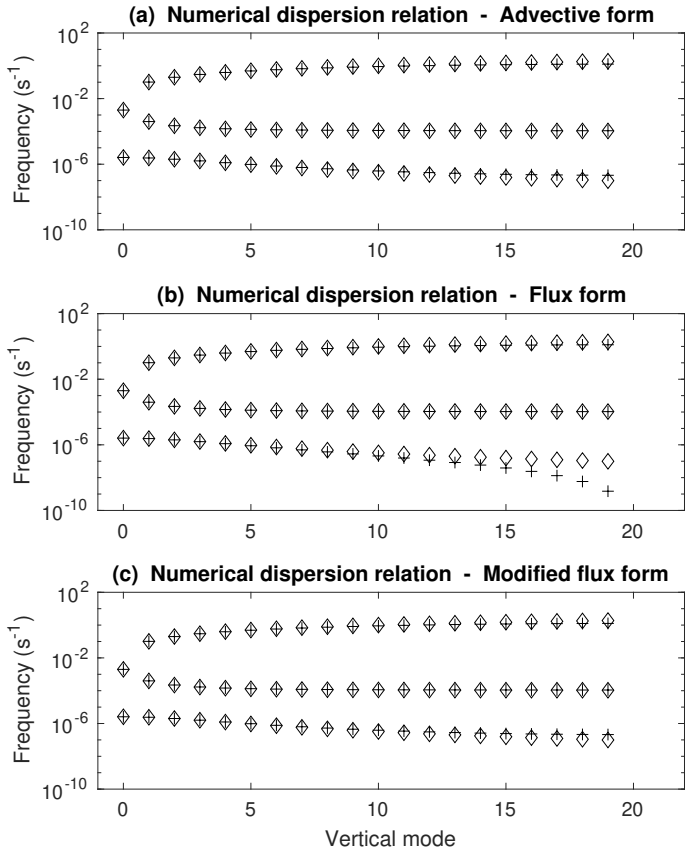

FIGURE 3 Numerical dispersion relation (crosses) and analytical dispersion relation (diamonds) showing frequency (s^{-1}) versus vertical mode number. (The mode number is equal to the number of zeros in the vertical structure of u.) The discrete entropy equation is (a) in advective form, (b) in the naive flux form (5) and (6), and (c) in the modified flux form (7) and (8). In each panel the three branches represent acoustic modes (highest frequency), inertia-gravity modes, and Rossby modes (lowest frequency), all westward propagating; there are also eastward propagating acoustic and gravity mode branches (not shown). The parameters used are as follows: domain depth 10 km; number of vertical levels 20; gravitational acceleration 9.80616 ms^{-2}; gas constant for dry air 287.05 $Jkg^{-1}K^{-1}$; specific heat capacity at constant pressure 1005 $Jkg^{-1}K^{-1}$; Coriolis parameter 1.031×10^{-4} s^{1}; northward gradient of Coriolis parameter 1.619×10^{-11} $s^{-1}m^{-1}$; background temperature 250 K; surface pressure 10^{5} Pa; zonal wavenumber $2\pi \times 10^{6}$ m^{-1}; meridional wavenumber zero.

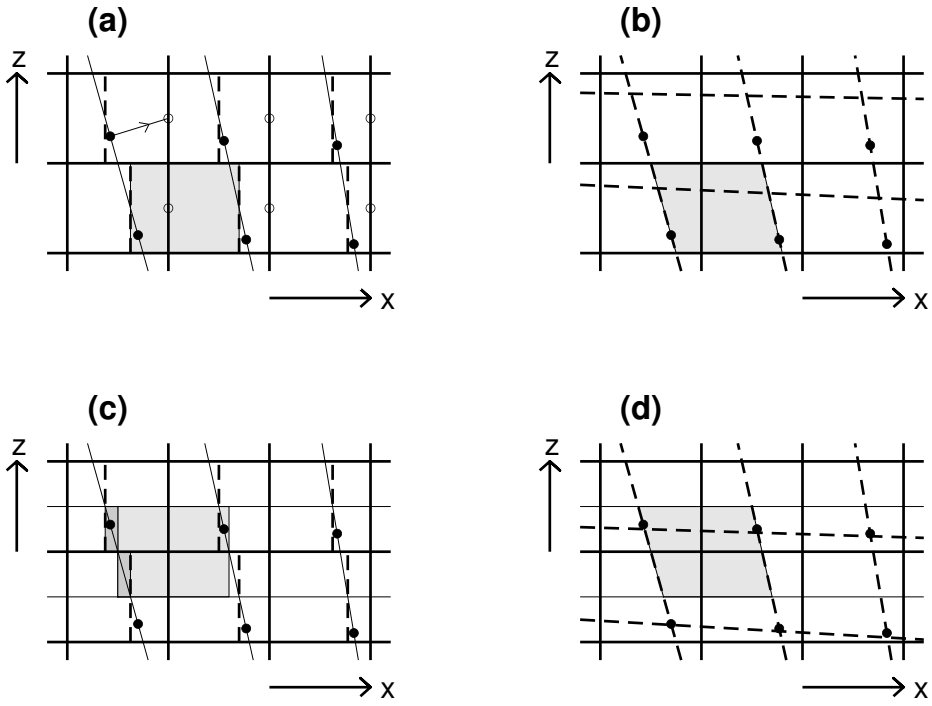

FIGURE 4 Schematic illustrating the modified SLICE scheme in two dimensions. The thick solid lines indicate the edges of the ρ-cells on the model grid. Filled circles indicate departure points for u-points and open circles, where shown, indicate u-points themselves. One of the u-point trajectories is shown in panel (a). (a) The dashed vertical lines indicate the lateral edges of the ρ-cell Intermediate Eulerian Control Volumes; one of the Intermediate Eulerian Control Volumes is shaded. In the first stage of SLICE the ρ field is remapped in the x-direction from the model grid ρ-cells to the corresponding Intermediate Eulerian Control Volumes. (b) Intermediate Lagrangian Control Volumes corresponding to ρ-cells are bounded at the sides by dashed lines and above and below by solid lines; one of these Intermediate Lagrangian Control Volumes is shaded. Departure volumes are bounded by dashed lines. The mass in an Intermediate Lagrangian Control Volume is assumed to equal the mass in the corresponding Intermediate Eulerian Control Volume. In the second stage of SLICE ρ is remapped quasi-vertically from Intermediate Lagrangian Control Volumes to departure volumes. Finally the mass in each departure volume is assumed to be transported during the time step to the corresponding arrival grid cell. (c) The light shaded rectangular region indicates one of the η-cell Intermediate Eulerian Control Volumes. In the first stage of SLICE $\overline{\rho}\eta$ is remapped in the x-direction from the model grid η-cells to the corresponding Intermediate Eulerian Control Volumes. In the modified SLICE scheme, a 'mass flux' difference is then estimated at the lateral faces of the Intermediate Eulerian Control Volumes and, combined with an estimate for $\partial\eta/\partial z$, is used to conservatively shift entropy between neighbouring Intermediate Eulerian Control Volumes. The two dark shaded regions indicate the regions used to compute this correction at one lateral face. (d) Intermediate Lagrangian Control Volumes corresponding to η-cells are bounded at the sides by dashed lines and above and below by thin solid lines; one of these Intermediate Lagrangian Control Volumes is shaded. η-cell departure volumes are bounded by dashed lines. The entropy content in an Intermediate Lagrangian Control Volume is assumed to equal the entropy content in the corresponding Intermediate Eulerian Control Volume. In the second stage of SLICE η is remapped quasi-vertically from Intermediate Lagrangian Control Volumes to departure volumes. Finally the entropy content in each η-departure volume is assumed to be transported during the time step to the corresponding arrival η-cell.

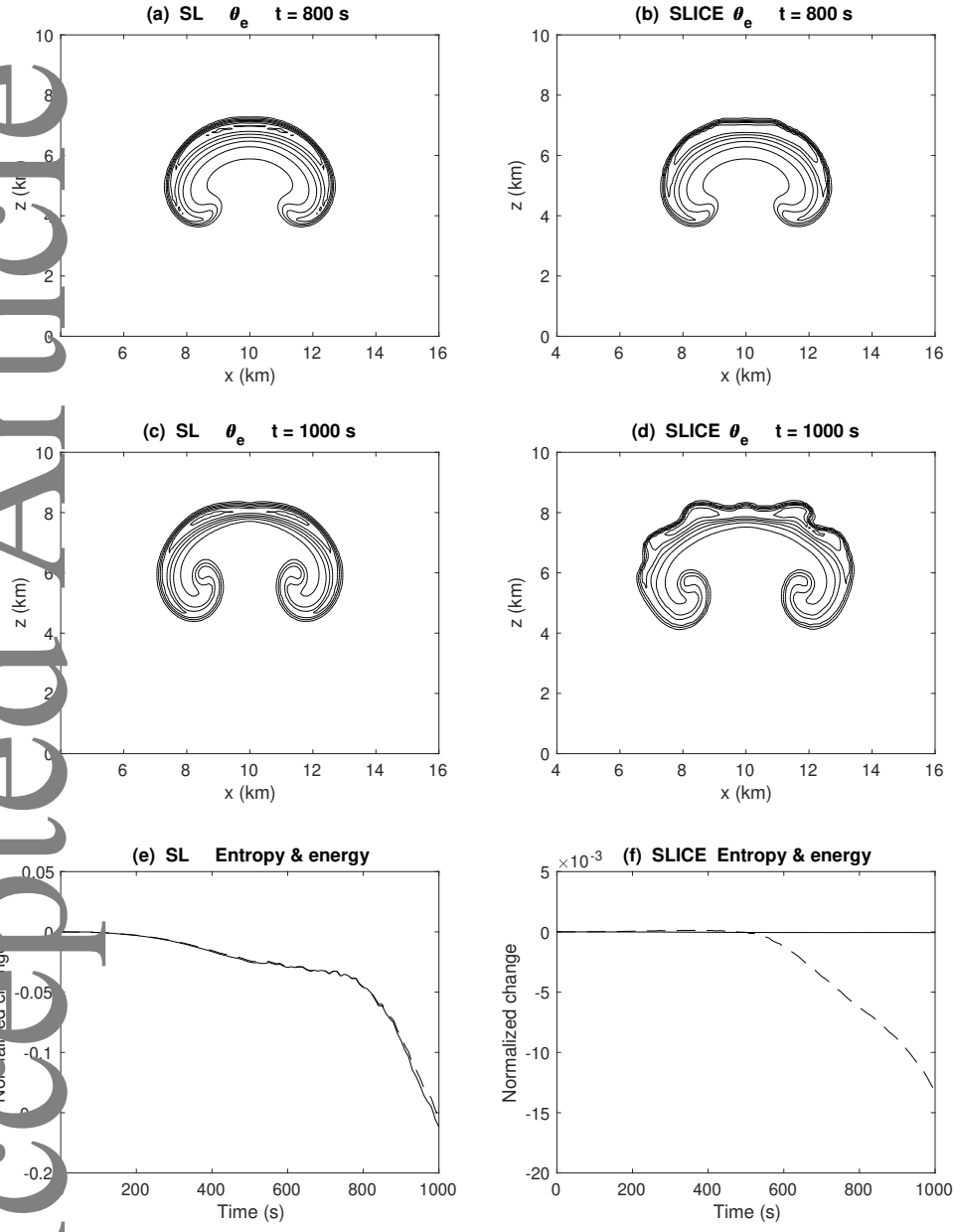

FIGURE 5 Results for the Bryan and Fritsch (2002) saturated buoyant bubble test case. Panels (a), (c) and (e) are for semi-Lagrangian advection of entropy, specific humidity, and w; panels (b), (d) and (f) are for modified SLICE advection of entropy, specific humidity, and w. Panels (a) and (b) show the equivalent potential temperature perturbation after 800 s while panels (c) and(d) show the equivalent potential temperature perturbation after 1000 s. The contour interval is 0.5 K. The domain is 20 km wide; only the middle portion is shown. Panels (e) and (f) show time series of the normalized change in domain-integrated entropy (solid) and domain-integrated energy (dashed); note the different axis scales in panels (e) and (f).